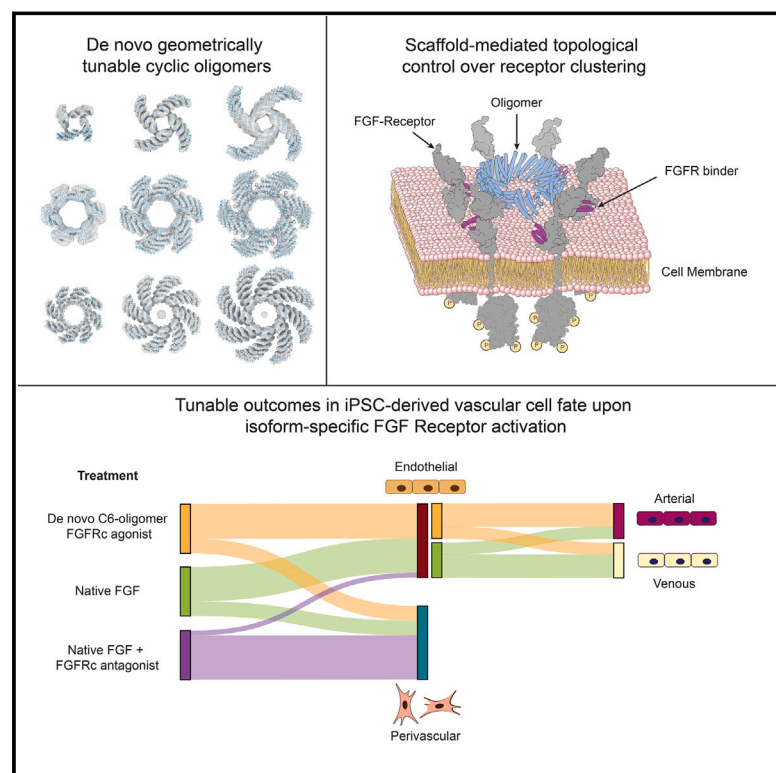# Modulation of FGF pathway signaling and vascular differentiation using designed oligomeric assemblies

Graphical abstract

Authors

Natasha I. Edman, Ashish Phal, Rachel L. Redler, ..., Gira Bhabha, Hannele Ruohola-Baker, David Baker

Correspondence

hannele@uw.edu (H.R.-B.), dabaker@uw.edu (D.B.)

In brief

De novo designed synthetic agonists against the c-isoform of the FGF receptor are used to specifically control cellular fate in a vascular endothelial cell differentiation model.

Highlights

- *De novo* designed cyclic oligomers with tunable geometric properties

- Oligomeric FGFR-binding modules induce geometry- and valency-dependent signaling

- Modulation of FGFR isoform activity controls cell fate during vascular development

- FGFR c-isoform activation favors arterial fate, while b-isoform favors perivascular fate

Cell

Article

Modulation of FGF pathway signaling and vascular differentiation using designed oligomeric assemblies

Natasha I. Edman,[1,2,3,4,20] Ashish Phal,[5,6,20] Rachel L. Redler,[7,20] Thomas Schlichthaerle,[1,2,20] Sanjay R. Srivatsan,[2,4,8] Devon Duron Ehnes,[1,5] Ali Etemadi,[1,2,9] Seong J. An,[10] Andrew Favor,[1,2] Zhe Li,[1,2] Florian Praetorius,[1,2] Max Gordon,[1,5] Thomas Vincent,[5,6,11] Silvia Marchiano,[5] Leslie Blakely,[5] Chuwei Lin,[8] Wei Yang,[1,2] Brian Coventry,[1,2] Derrick R. Hicks,[1,2] Longxing Cao,[1,2] Neville Bethel,[1,2,12] Piper Heine,[1,2] Analisa Murray,[1,2] Stacey Gerben,[1,2] Lauren Carter,[1,2] Marcos Miranda,[1,2] Babak Negahdari,[9] Sangwon Lee,[10] Cole Trapnell,[8,13,14] Ying Zheng,[5,6,15] Charles E. Murry,[5,6,15,16,17] Devin K. Schweppe,[8] Benjamin S. Freedman,[5,6,11,13,16,18] Lance Stewart,[1,2] Damian C. Ekiert,[7,19] Joseph Schlessinger,[10] Jay Shendure,[8,12,13,14] Gira Bhabha,[7] Hannele Ruohola-Baker,[1,5,6,8,21,*] and David Baker[1,2,12,*]

[1]Department of Biochemistry, University of Washington, Seattle, WA 98195, USA
[2]Institute for Protein Design, University of Washington, Seattle, WA 98195, USA
[3]Molecular and Cellular Biology Graduate Program, University of Washington, Seattle, WA 98195, USA
[4]Medical Scientist Training Program, University of Washington, Seattle, WA 98195, USA
[5]Institute for Stem Cell and Regenerative Medicine, University of Washington, Seattle, WA 98109, USA
[6]Department of Bioengineering, University of Washington, Seattle, WA 98195, USA
[7]Department of Cell Biology, New York University School of Medicine, New York, NY 10016, USA
[8]Department of Genome Sciences, University of Washington, Seattle, WA 98195, USA
[9]Medical Biotechnology Department, School of Advanced Technologies in Medicine, Tehran University of Medical Sciences (TUMS), Tehran, Iran
[10]Department of Pharmacology, Yale University School of Medicine, New Haven, CT 06520, USA
[11]Division of Nephrology, Department of Medicine, University of Washington School of Medicine, Seattle, WA 98109, USA
[12]Howard Hughes Medical Institute, University of Washington, Seattle, WA 98195, USA
[13]Brotman Baty Institute for Precision Medicine, Seattle, WA 98195, USA
[14]Allen Discovery Center for Cell Lineage Tracing, Seattle, WA 98109, USA
[15]Center for Cardiovascular Biology, University of Washington, Seattle WA 98109, USA
[16]Department of Laboratory Medicine and Pathology, University of Washington, Seattle, WA 98195, USA
[17]Department of Medicine/Cardiology, University of Washington, Seattle WA 98195, USA
[18]Kidney Research Institute, University of Washington School of Medicine, Seattle, WA 98109, USA
[19]Department of Microbiology, New York University School of Medicine, New York, NY 10016, USA
[20]These authors contributed equally
[21]Lead contact
*Correspondence: hannele@uw.edu (H.R.-B.), dabaker@uw.edu (D.B.)
https://doi.org/10.1016/j.cell.2024.05.025

SUMMARY

Many growth factors and cytokines signal by binding to the extracellular domains of their receptors and driving association and transphosphorylation of the receptor intracellular tyrosine kinase domains, initiating downstream signaling cascades. To enable systematic exploration of how receptor valency and geometry affect signaling outcomes, we designed cyclic homo-oligomers with up to 8 subunits using repeat protein building blocks that can be modularly extended. By incorporating a *de novo*-designed fibroblast growth factor receptor (FGFR)-binding module into these scaffolds, we generated a series of synthetic signaling ligands that exhibit potent valency- and geometry-dependent Ca^{2+} release and mitogen-activated protein kinase (MAPK) pathway activation. The high specificity of the designed agonists reveals distinct roles for two FGFR splice variants in driving arterial endothelium and perivascular cell fates during early vascular development. Our designed modular assemblies should be broadly useful for unraveling the complexities of signaling in key developmental transitions and for developing future therapeutic applications.

INTRODUCTION

Clustering of cell surface receptors can enhance and sustain activation in response to an extracellular signal, and there is considerable interest in technologies to manipulate receptor clustering.[1–6] Designed protein assemblies have previously been used to drive receptor clustering using naturally occurring receptor-binding domains,[7–9] and geometrically tunable dimeric

ligands have been used to probe the influence of dimerization geometry on signaling output.[10–13] Higher-order receptor assemblies are thought to function in a variety of signaling systems[14–16]; a tunable oligomeric scaffold presenting receptor-binding domains would facilitate studies into the effect of angstrom-level topology on receptor output. Previous design efforts have generated oligomers with a variety of cyclic symmetries,[17–20] but these proteins were not easily modifiable to produce distinct receptor-binding configurations.

Fibroblast growth factor (FGF) receptors (FGFRs) are tyrosine kinases that play critical roles in embryonic development and cancer. The pathway is complex and highly regulated, with four FGF receptor genes and two isoforms generated by alternative splicing of exon 8 vs. exon 9, which alter the third immunoglobulin (Ig)-like domain (D3), generating receptor isoforms IIIb and IIIc (referred to as "b" and "c," respectively, throughout the text).[21–23] Although D3 is part of the FGF-binding region, and the receptor isoforms have different affinities for the various FGF ligands, the contribution of the two isoforms to proper tissue differentiation is not fully understood.[24] The c-isoform is amplified in many solid carcinomas and hence may be a target for cancer therapy.[22]

Here, we describe the *de novo* design of geometrically tunable cyclic oligomers to overcome the limitations of current scaffolding systems and the use of these synthetic scaffolds with an FGFR c-isoform-specific-designed minibinder[21] to probe and manipulate vascular differentiation.

RESULTS

De novo oligomer design

Cyclic oligomers (Cx, with "x" denoting valency) were designed using a set of 18 designed helical repeat proteins (DHRs), each consisting of four identical repeats of a two-helix module and with high-resolution crystal structures or small-angle X-ray (SAXS)[25,26] spectra consistent with the corresponding design models (Table S1; Figure S1A). We docked each DHR into C4, C5, C6, C7, and C8 cyclic oligomeric assemblies and evaluated them using the protein-backbone-based residue-pair transform (RPX) metric, which assesses interface designability (Figure S1B).[20,27] For the top-scoring docks, the residue identities and conformations at the homo-oligomeric interface were optimized using RosettaDesign to favor oligomer assembly. We filtered for designs with a high solvent-accessible surface area (SASA > 700 $Å^2$), favorable free energies of assembly ($\Delta\Delta G$ between −35 and −70), high shape complementarity (sc > 0.65), and interfaces with fewer than 2 unsatisfied hydrogen bonds.[28,29] A total of 109 designs were selected for structural characterization: 15 tetramers, 16 pentamers, 24 hexamers, 24 heptamers, and 30 octamers. A second set of designs using a computational library of 1,526 5-helix concave scaffolds (5HCS)[30,31] were docked with C2 symmetry, and from 3,747 C2 oligomers, 14 designs were selected for further analysis (Figure S1C).

Design characterization

Synthetic genes encoding the 109 designs of symmetry C4 or higher were synthesized, expressed as protein in *Escherichia*

coli, and purified using immobilized metal affinity chromatography (IMAC). Of the 60 designs that were soluble, 28 had single monodisperse peaks on size exclusion chromatography (SEC). Of these, ten designs were found to have a single oligomeric state by both SAXS[32–34] and SEC with multi-angle light scattering (SEC-MALS). Five of the successes were tetramers, four were hexamers, and one was an octamer. From the 14 C2 designs, 3 (C2-58, C2-CDX, and C2-Y2D) had soluble expression, were confirmed to have a monodisperse peak on SEC, and had a correctly assembled oligomeric state verified by SAXS and SEC-MALS (Figure S2; Table S2).

The varied topology of the repeat protein building blocks enabled us to create oligomers with distinct arm orientations. The starting scaffold DHR71 generated 5 successful designs (C4-71, C4-717, C6-71, C6-714, and C8-71), with a variety of interface geometries that permitted this building block to assume 3 distinct valencies. C4-71 and C4-717, for example, contain changes in different sets of residues that result in distinct oligomer geometries. In contrast, the designs C4-71, C6-71, and C8-71 employ a similar backbone region as the oligomeric interface, yet adopt different oligomeric states (Figure S3). C4-181 utilizes DHR18 as the single-chain building block and is docked together at the C-terminal helices, yielding an inner cavity diameter of 45.6 Å (C-terminal distance of opposing chains, Figure 1A). C4-717 is tightly docked together at the C-terminal helices, creating a purely hydrophobic core between all four chains (Figure 1B). C6-714 has an inner cavity diameter of 43.2 Å and its N terminus can be extended to achieve larger distance spacing, whereas the structure is again docked together at the C terminus (Figure 1C). C6-46 involves the carboxyl (C)- and amino (N)-terminal helices at the interfaces to adjacent chains, where the N terminus points toward the central cavity and the C terminus toward the outside (Figure 1D). The designed residue substitutions that generate the oligomeric assemblies from the original DHR building blocks are listed in Table S3. Six designs were further selected for characterization by cryoelectron microscopy (cryo-EM) (Tables S4 and S5). The cryo-EM map for windmill-shaped C4-131 was limited to >10 Å global resolution due to preferred orientation bias, but shows that the "blades" are arranged as designed and that the four core C-terminal helices are tightly packed (Figure 1E). The higher resolution for design C4-81 allows individual helices to be clearly distinguished, and following rigid-body fitting using ChimeraX, the design model closely matched the cryo-EM map (Figure 1F). For C6-79, a C6-docked assembly matched the SAXS data more closely than the original C8 assembly as well as the cryo-EM map, and the 2D classes clearly indicate that it is a hexamer under our cryo-EM conditions (Figure 1G).

Oligomer extension

An advantage of using modular repeat proteins as building blocks is that the length of the oligomer arms can be increased or decreased simply by inserting or deleting repeat units (Figure 2A).[10,20,25] To explore the viability of this approach, three designs (C4-71, C6-71, and C8-71) derived from DHR71 were selected for repeat extension. Two or four repeat units were added at the N terminus, creating a 6-repeat variant and an 8-repeat variant of each design. The oligomeric state of each
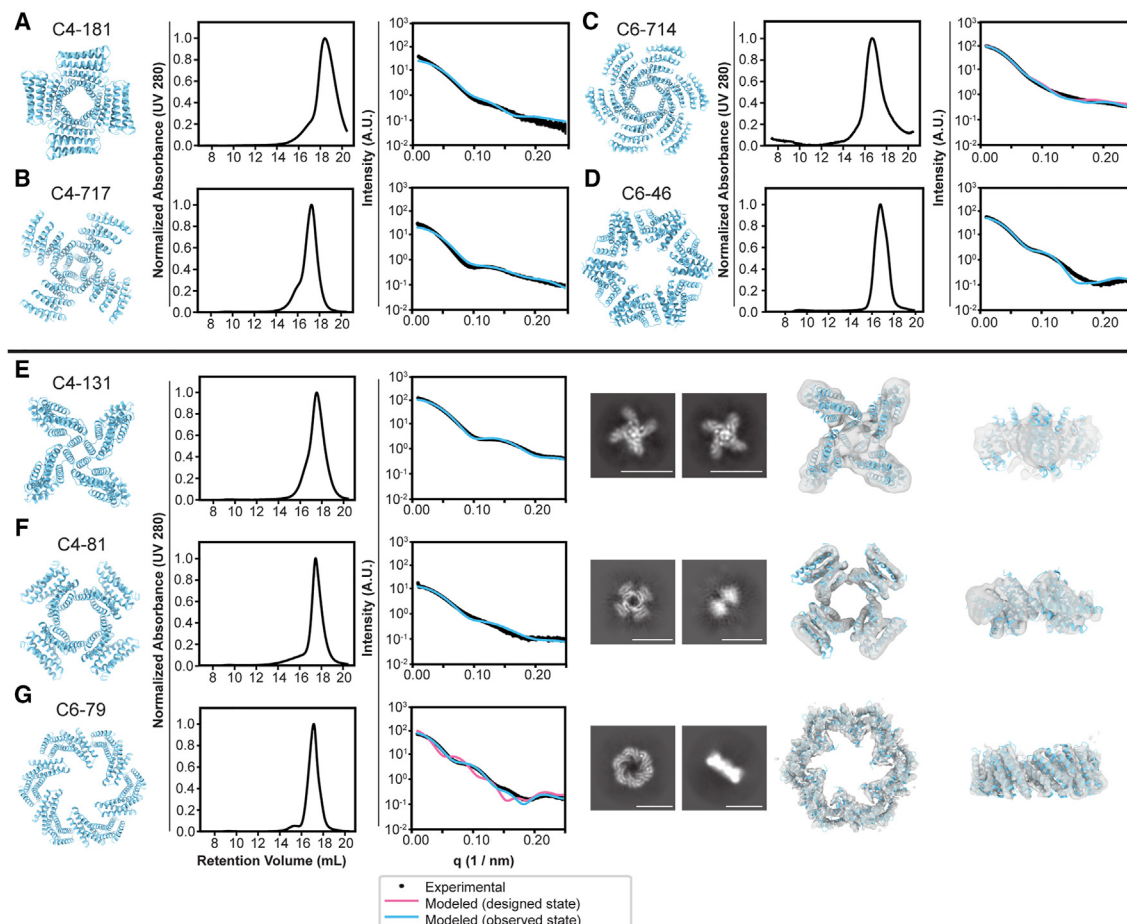
Figure 1. Biophysical characterization of designed protein oligomers
From left to right: design model, size-exclusion chromatogram, and SAXS data comparison of model to experimental data (A) C4-181, (B) C4-717, (C) C6-714, (D) C6-46, and (E) C4-131 design model, size-exclusion chromatogram, and SAXS data analysis; right: cryo-EM 2D class average, cryo-EM map (EMDB: EMD-28958) overlay to design model (cyan) top and side view (F) C4-81 design model, size-exclusion chromatogram, SAXS data analysis; right: cryo-EM 2D class average, cryo-EM map (EMDB: EMD-28973) superimposed to design model (cyan) top and side view (G) C6-79 SEC characterization and SAXS fit using both the C8 design model and the C6 dock. Right: cryo-EM 2D class average, cryo-EM map (EMDB: EMD-28889) superimposed to design model top and side view. Scale bars: 10 nm in (E)–(G).
See also Figures S1, S2, and S5 and Tables S1–S5.

extended design was characterized by SEC-MALS, SAXS, and cryo-EM. Both 2D classes and 3D reconstructions from single-particle cryo-EM analysis of the extended oligomers show overall geometry in good agreement with design models, with sufficiently high resolution in some cases to confirm positions of individual helices. The C-terminal helix of C4-71 docked as designed against the mid-axis of the neighboring chain horizontally, yielding a distance of 47.4 Å between opposing-chain C termini across the inner cavity (Figure 2B; the interface harbors 10 tryptophans, which make pi-pi stacking interactions stabilizing the assembly). C6-71, in contrast, has an inner diameter of 72.0 Å between opposing-chain C termini and harbors a tilted chain-chain interaction, where the interfacial C-terminal helix is only in contact with the neighboring chain along half its length. Side-chain orientations can be discerned in the C6-71 8-repeat extension map despite the low number of total particles used in constructing this map (Figure 2C). The octopus-like C8-71 structure has N-ter-

minal extensible arms with C-terminal helices of the individual chains docked together along the full horizontal length of the structure, resulting in an inner diameter of 55.1 Å and a maximal distance between opposing N termini of 170.0 Å in the largest 8-repeat extension (Figure 2D).

All cryo-EM maps were in good agreement with the respective design models, with the exception of C6-79, which, as noted above, formed a hexamer instead of the designed octamer. None of the other designs showed any off-target oligomeric states in the 2D class averages (Figures S4–S8).

Cryo-EM reconstructions of C6-79 and C8-71
Based on the resolution of the cryo-EM maps, we built models for C6-79 and C8-71 (Figures S9–S11; Table S6). Both the C6-79 and C8-71 cryo-EM models align well with the corresponding design models, with pairwise root-mean-square deviations (RMSDs) of 2.85 and 1.79 Å, respectively (Figure 3).
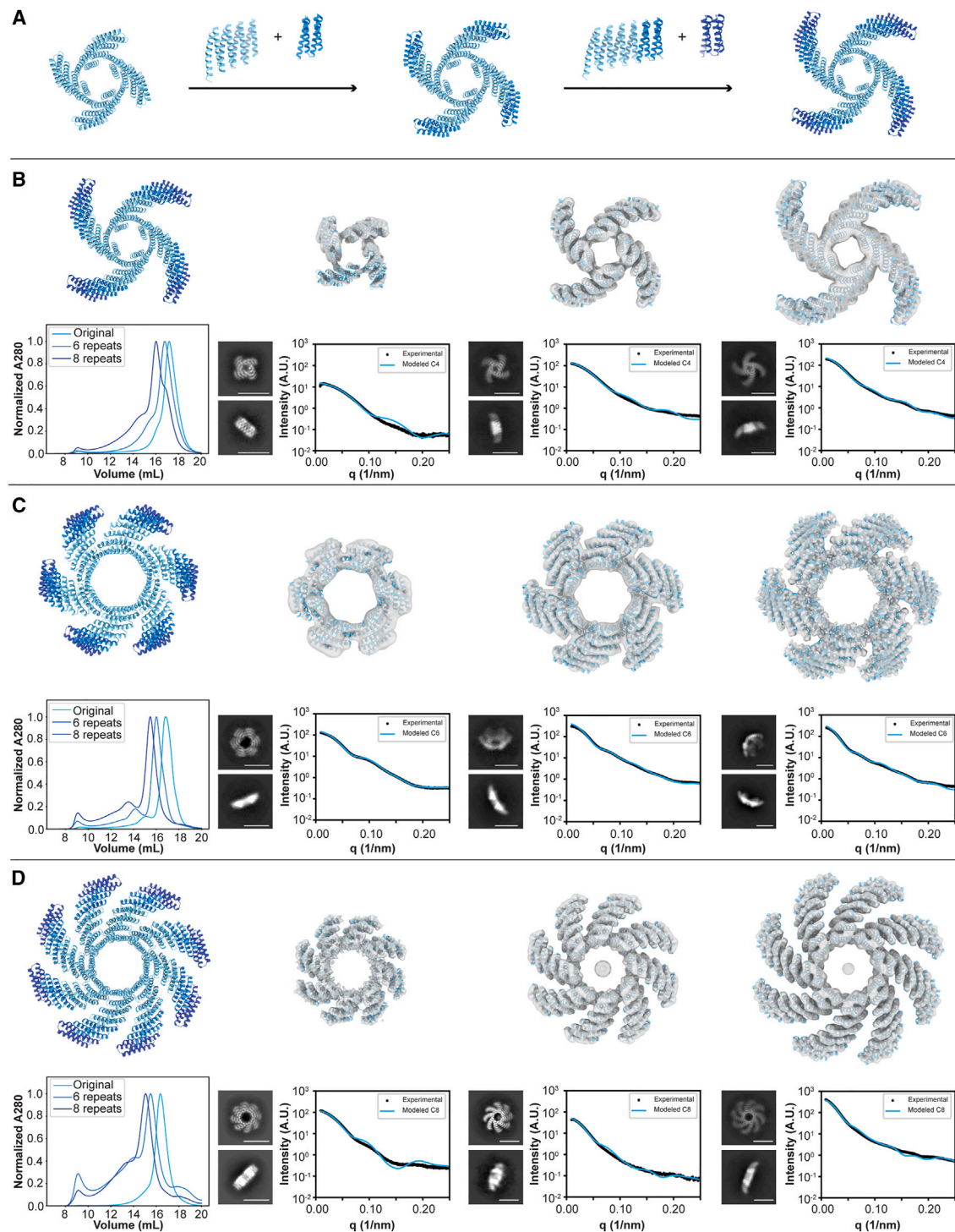
Figure 2. Modulating oligomer geometry by repeat extension

(A) Depiction of DHR-based repeat extension for oligomers. Each extension unit consists of 2 repeats.

(B) C4-71 4-repeat (EMDB: EMD-28974), 6-repeat (EMDB: EMD-28966), and 8-repeat (EMDB: EMD-28967) cryo-EM maps superimposed with design model, top and side-view class averages and SAXS characterization below the cryo-EM maps of the different repeat extension variants. Bottom left: SEC overlay of the individual structures.

(C) C6-71 4-repeat (EMDB: EMD-28968), 6-repeat (EMDB: EMD-28969, and 8-repeat (EMDB: EMD-28970) cryo-EM maps superimposed with design model, top and side-view class averages and SAXS characterization below the cryo-EM maps of the different repeat extension variants. Bottom left: SEC overlay of the individual structures.

(legend continued on next page)

In C8-71, the hydrophobic residues Trp152 and Leu198 on the adjacent chain are buried in the interface or the core of the structure, respectively, and are important for interface formation (Figure S12A). Mutating these residues to hydrophilic residues (W152E and/or L198D) disrupts oligomer formation, as shown by broadening of the SEC trace (Figure S12B).

Design of FGFR agonists

We next investigated whether clustering receptor tyrosine kinases in higher-order geometries by presenting receptor-binding domains on the designed oligomers could drive cross-phosphorylation of their intracellular kinase domains and induce downstream signaling.[35] The multiple distinct valencies and geometries of our oligomeric ligands enable exploration of how the geometry and valency of tyrosine kinase receptor association influence signaling output and cell behavior (Figure 4A, left). We chose as a model system the FGF signaling pathway (Figure 4A, right) and fused a *de novo*-designed minibinder (mb7) against FGFRc (PDB: 7N1J) at either the N or C termini of the designed cyclic oligomers with a short glycine-serine linker.[36] Six oligomers were selected for fusion: C2-58, C4-71, C6-71, C6-79, and C8-71. Depending on the fusion terminus and the geometry of the oligomer, the binding domains are displayed at different spacings on adjacent subunits: for example, C6-79C_mb7 displays the minibinders 54 Å apart with mb7 on the C terminus of the oligomer, while C6-79N_mb7 displays the binders 18 Å apart with mb7 on the N terminus of the oligomer. In SEC experiments, the fusions eluted at the same volume as the base oligomers, with the exception of C6-71C_mb7, which eluted significantly earlier than the base design. 2D EM class averages showed that C6-71C_mb7 particles were self-associating into dihedral structures, presumably via the hydrophobic interface of the minibinder domain being presented in a favorable conformation for this interaction. The other oligomeric fusions showed little to no self-association on EM or SEC (Figure S13).

FGFR pathway activation

FGF-mediated FGFR signaling results in stimulation of the Ras signaling pathway, leading to phosphorylation of extracellular-signal-regulated kinase 1 and 2 (ERK1/2) and activation of phospholipase C-gamma (PLC-γ), leading to intracellular calcium release.[24,37,38] We evaluated the signaling activity of our designs by screening them in serum-starved Chinese hamster ovary (CHO) cells stably expressing hFGFR1c (CHO-R1c) at 10 nM each for 15 min at 37°C. Downstream activation through phosphorylation of ERK1/2 and FGFR1 (Y653/654) was analyzed by western blot. Of the designs, we found that C6-79C_mb7, C6-79N_mb7, C4-71N_mb7, C4-71C_mb7, and C8-71C_mb7 broadly induced strong FGFR activation and ERK1/2 phosphorylation, comparable to that achieved by native FGF2, while C2-58-2X_mb7, C6-71C_mb7, C6-71N_mb7, and C8-71N_mb7 displayed weaker activity (Figures 4B and S14).

To characterize their dose-dependent activity, we titrated a subset of these designs using phosphoflow[39] and western blotting for ERK1/2 phosphorylation in CHO-R1c cells (Figures 4C and S15). C2-58-2X_mb7, C4-71C_mb7, C4-71N_mb7, C6-79C_mb7, and C8-71C_mb7 had similar EC_{50} values of 0.63, 1.33, 0.89, 1.56, and 2.07 nM, respectively, and similar maximal activation (E_{max}) values, while C2-58-2X_mb7 had a lower E_{max}. To investigate how the geometry of receptor association influences signaling, the rigid repeat arm length of C4-71N_mb7 was systematically varied, leading to distances between mb7 N termini of 53, 76, and 96 Å. Phosphoflow experiments showed that only the shortest separation distance (53 Å) was able to stimulate ERK phosphorylation (with an EC_{50} of 1.3 nM), whereas the larger separation distances of mb7 did not lead to pathway activation (Figure S16).

Receptor clustering on the cell surface

To investigate whether FGFR1c activation was due to induced receptor clustering, cells were examined by single-particle tracking with a HaloTag targeting FGFR1c[40] to directly visualize their diffusion in the plasma membrane; receptors engaged in a signaling cluster should exhibit decreased diffusion, manifesting in a decreased diffusion coefficient.[41] Receptors on cells treated with C6-79C_mb7 showed slower diffusion than those treated with FGF1 and heparin (Figure S17), indicating that C6-79C_mb7 induces an oligomeric state of FGFR1c at the membrane. To probe the presence of local receptor clusters on the cell surface after ligand treatment, intensity levels of single spots in HaloTagged CHO-R1c cells labeled with Alexa488 were evaluated.[42] C6-79C_mb7-treated cells showed signals with an intensity distribution slightly shifted compared with FGF1 supplemented with heparin, with intensity peaks at 500, 1,000, and 2,000 a.u., suggesting that multiple receptors are clustered together by the designed mb7-presenting oligomers. The extent of signaling correlated with the ability of the designs to cluster receptors (Figures 4D and 4E).

FGFR1c isoform specificity

FGFRs 1–3 have two alternatively spliced variants, the "c" and "b" isoforms, which have different third Ig-like domains and variable FGF ligand affinities.[43] Tissue-specific expression of these isoforms and their reciprocal signaling play roles in embryonic development, tissue repair, and cancer.[22] Separating the functions of the FGFR b- and c-isoforms in differentiation has been hindered by a lack of ligands that can selectively bind one isoform or the other. The mb7 minibinder was designed to specifically bind the c-isoform of the FGFR, and it selectively inhibits signaling through this isoform.[21] We evaluated the receptor isoform specificity of our synthetic agonists by treating serum-starved L6 rat myoblast cells stably expressing either the c- or b-isoform of hFGFR1 (L6-R1c or L6-R1b, respectively; overexpression was validated with RT-qPCR [Figure S18]) with 10 nM

(D) C8-71 4-repeat (EMDB: EMD-28888), 6-repeat (EMDB: EMD-28971), and 8-repeat (EMDB: EMD-28972) cryo-EM maps superimposed with design model, top and side-view class averages and SAXS characterization below the cryo-EM maps of the different repeat extension variants. Bottom left: SEC overlay of the individual structures. Scale bars: 10 nm in (B)–(D).
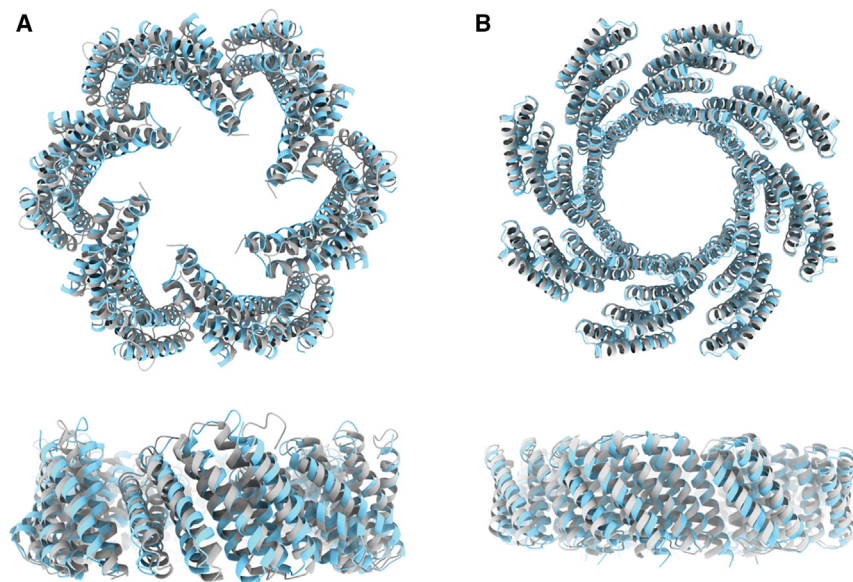See also Figures S3, S4, and S6–S8 and Tables S2–S5.

Cell
Article

Figure 3. Cryo-EM structural analysis
(A) C6-79 alignment of design model (gray) with cryo-EM structure (cyan, PDB: 8F6R) in top and side view. Structures align well with an RMSD of 2.85 Å (B) C8-71 alignment of design model (gray) with cryo-EM structure (cyan, PDB: 8F6Q) in top and side view. Structures are in good agreement with an RMSD of 1.79 Å.
See also Figures S9–S12 and Tables S4–S6.

Sculpting vascular differentiation with the designed agonists

FGF signaling plays an important role during early embryogenesis[44,45]; the controlled spatiotemporal expression of FGFRs and their ligands drives specification and development of many cell lineages.[46–48] In the vasculature, mesodermal precursors give rise to endothelial and perivascular cell fates. The role of FGF signaling and the FGFR isoforms in this bifurcation is not currently understood.

of mb7, FGF2, or C6-79C_mb7 for 15 min at 37°C. Although FGF2 does not discriminate between the two FGFR1 isoforms and activates signaling in both cell types, C6-79C_mb7 stimulates ERK1/2 and FGFR phosphorylation only in L6-R1c cells. We reasoned that it should be possible to specifically activate signaling through the b-isoform by combining FGF2 with the monomeric mb7 (which blocks signaling through the c-isoform); to test this, we stimulated both L6 cell lines with a combination of mb7 and FGF2 at 10 nM each for 15 min. We found that this combination stimulates ERK1/2 phosphorylation in L6-R1b cells only; thus, our designs enable selective activation of signaling through either isoform (Figure 4F).

We next investigated the ability of the designs to activate FGF signaling through the PLC-γ downstream branch of signaling by measuring the levels of intracellular calcium release following treatment of serum-starved CHO-R1c cells with varying concentrations of the designs. These results show a similar trend: C6-79C_mb7, C4-71C_mb7, and C8-71C_mb7 induce strong intracellular calcium release, with EC_{50} values of 0.38, 0.72, and 3.09, respectively, while C2-58-2X_mb7 displays lower activity, with an EC_{50} of 26.02 nM (Figures 4G and S19). Although the peak magnitude of calcium release was similar between FGF2 at 10 nM and the synthetic agonist C6-79C_mb7 at 10 nM, there was a pronounced difference in the duration of the response: the higher valency synthetic ligand, C6-79C_mb7, generated longer-duration calcium transients (Figure 4H), similar to a control condition in which we supplemented FGF2 together with heparin. This strong, heparin-independent signaling effect (Figure S20) of our designed agonist likely reflects the slow off rates of the high avidity multivalent agonists (Figure S21). To compare the effects of the agonist C6-79C_mb7 and FGF2 on the whole proteome, we carried out a (phospho-)proteomic analysis using mass spectrometry following treatment of FGFR1c-expressing CHO cells and found very similar changes in the overall proteome and in phosphopeptide abundance (Figure S22).

We investigated the effect of the c-isoform-specific FGFR minibinder oligomers on vascular development by generating endothelial cells and perivascular cells from human induced pluripotent stem cells (iPSCs) through a cardiogenic mesoderm intermediate (Figure S23A).[49] We replaced the ∼1 nM FGF2 (which engages both b- and c-isoforms of FGFRs[50]) in a previously described differentiation media between days 2 and 5 (when mesodermal intermediates first appear) in the protocol with 1 nM C6-79C_mb7 (the most potent synthetic agonist), 100 nM C2-58-2X_mb7 (the weakest agonist), 10 nM mb7, or 10 nM mb7, in combination with 1 nM FGF2 (to specifically activate signaling through the b-isoform), and from day 5 onward allowed the cells to differentiate in normal conditions for 28 days; samples were harvested for single-cell RNA sequencing (scRNA-seq) analysis at days 0, 5, 14, and 28. The sequencing datasets were analyzed using Monocle3[51] and visualized using uniform manifold approximation and projection (UMAP), which revealed 5 clusters of cells that segregated predominantly by time point and cell type (Figure 5A); cell types were annotated based on the differential expression of previously published canonical marker genes (Figure S23B).

Endothelial versus perivascular fate specification
All treatments (FGF2 and designed agonists) directed iPSCs to differentiate and form a common endothelial-perivascular precursor at day 5. This common precursor population then bifurcated to form either endothelial cells or perivascular cells at day 14. The cellular differentiation trajectory was design-dependent and determined by day 14. Addition of FGF2, C6-79C_mb7, or C2-58-2X_mb7 generated ∼60% endothelial cells in all three cases; the remaining population differentiated into perivascular cells. In contrast, the differentiation media without any FGF addition (control) resulted in a population that was only ∼34% endothelial (endothelial cell formation is weakly driven in the absence of any supplemented FGF2, presumably because of low levels of endogenously secreted FGFs; Figure S23C). On the other end
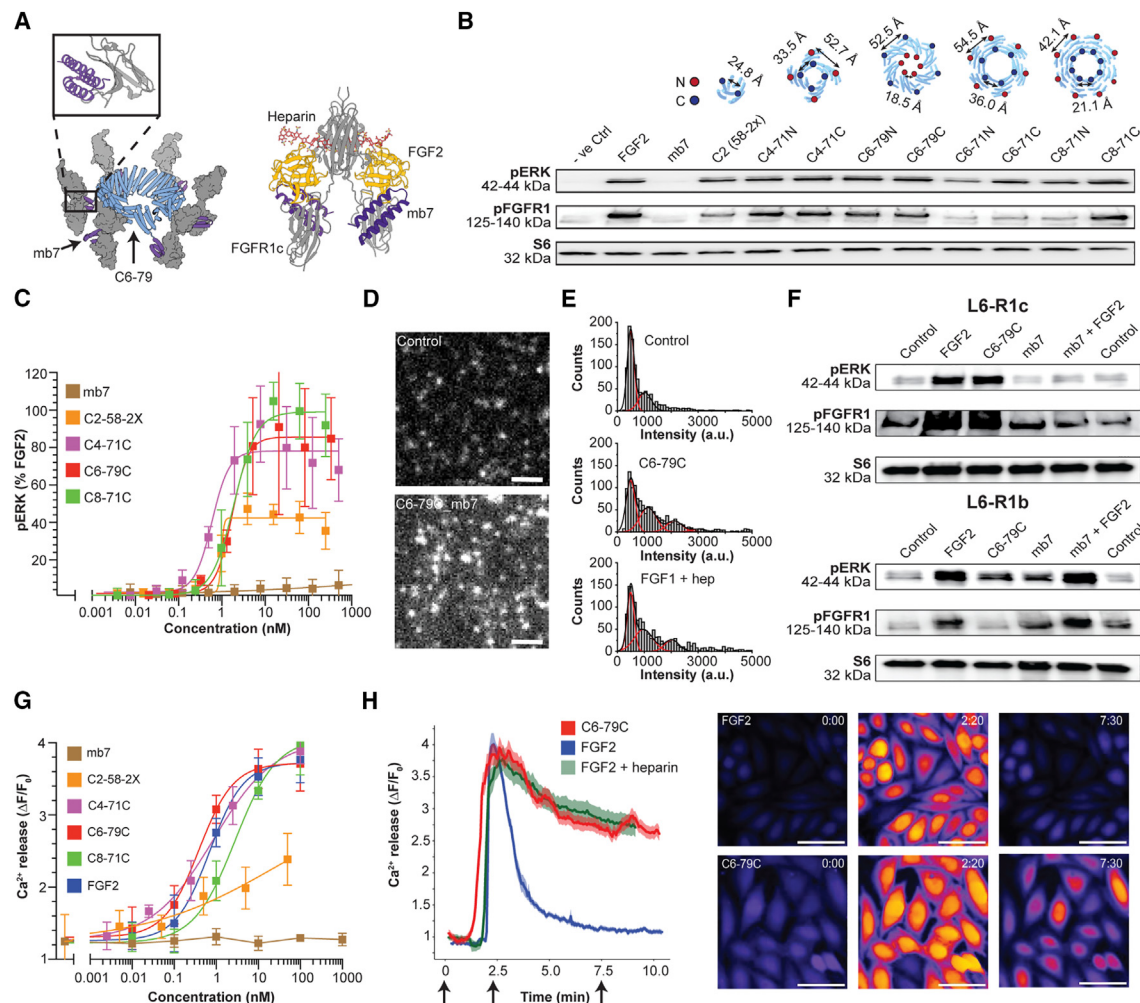
Figure 4. Modulation of FGFR signaling by designed agonists

(A) Cartoon model of C6-79C_mb7 oligomer (blue and purple) engaging six FGF receptors (gray). Top left: cartoon model of mb7 engaging FGFR4 domain 3 (PDB: 7N1J). Right: natural geometry of signaling competent FGF2 (yellow) with FGFR1c (gray) and heparin (red) (PDB: 1FQ9) together with superimposed mb7 (purple).

(B) Signaling response to a library of oligomers presenting mb7 in CHO-R1c cells, treated at 10 nM each, analyzed through western blot. Top: cartoons of oligomers presenting mb7 at their N or C termini; distances between neighboring chains are shown above their respective treatments. Total FGFR1 and ERK loading controls can be found in Figure S14.

(C) Dose-response curves of selected designs via phosphoflow for pERK1/2 stimulation. Error bars represent SEM from three independent biological repeats.

(D) Single-particle tracking of FGFR1 molecules on the cell surface.

(E) Intensity histograms of receptor clusters on the cell surface reveals receptor clustering induced via oligomerization.

(F) Signaling response (pERK and pFGFR1) to FGF2, mb7, C6-79C_mb7, or mb7 + FGF2 in L6-R1c (top) or L6-R1b (bottom) cells, analyzed through western blot.

(G) Dose-response curves of selected designs, assessed through intracellular calcium release. Error bars represent SEM from three independent biological repeats.

(H) Comparison of a calcium intensity signaling trajectory after treatment with FGF2 (with or without heparin) or C6-79C_mb7 at 10 nM each. Right: exemplary images comparing the calcium response exhibited in CHO-R1c cells following treatment with FGF2 or C6-79C_mb7 at 10 nM across three different time points (0:00, 2:20, and 7:30 min). Scale bars: 2 μm in (D) and 50 μm in (H).

See also Figures S13–S22.

of the spectrum, cells treated with mb7 showed a marked preference for perivascular lineage, producing only 28% endothelial cells. Cells treated with a combination of mb7 and FGF2 were almost exclusively mesenchymal, producing a population that was 93% perivascular (Figure 5B). These results suggest that FGFR c-isoform activity is critical for the development of endothelial cells, and specific activation of the b-isoform instead

biases the cells toward perivascular fate. Immunostainings of differentiated iPSCs for endothelial (CD31) and perivascular (PDGFR-B) markers at day 14 confirmed the primary cell fate after treatment with C6-79C_mb7 (FGFR c-isoform-specific signaling) or mb7 together with FGF2 (FGFR b-isoform-specific signaling), which led to the enrichment of endothelial or perivascular cells, respectively (Figure 5C).
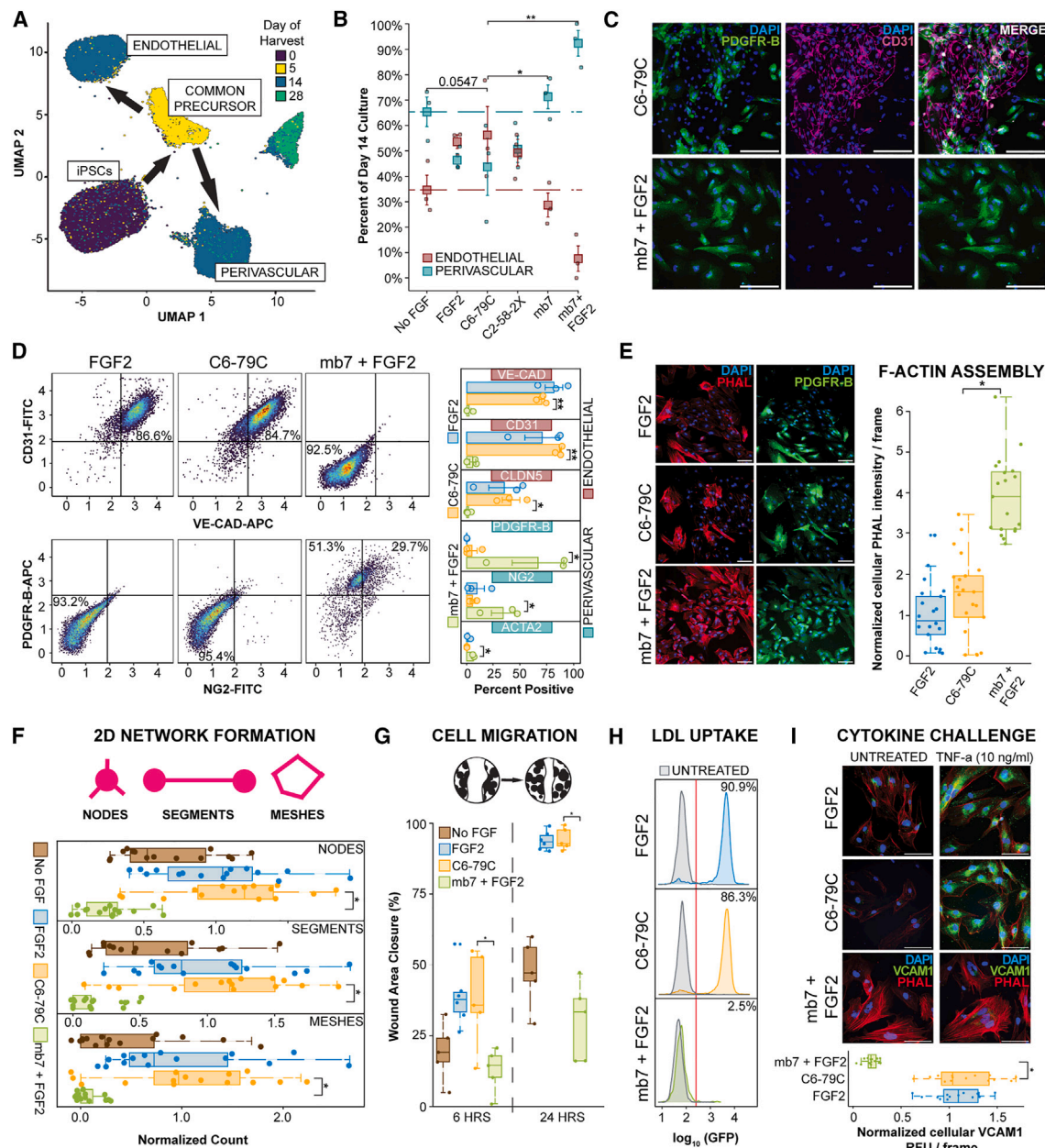
Figure 5. Control over vascular differentiation with designed agonists and antagonists

(A) UMAP embeddings of all sequenced cells colored by day of harvest, along with given cluster annotations.

(B) Proportion of endothelial or perivascular cells generated at day 14 following treatment with FGF2, C2-58-2X_mb7, C6-79C_mb7, mb7 alone, or mb7 in combination with FGF2. Error bars represent SEM from 3 independent biological repeats.

(C) Immunohistochemical characterization of differentiated cells treated with C6-79C_mb7 or mb7 in combination with FGF2, with PDGFR-B and CD31 to specifically mark perivascular and endothelial cells, respectively. Scale bars: 200 μm.

(D) Quantitative analysis of a select panel of endothelial (VE-cadherin, CD31, and CLND5) and perivascular (PDGFR-B, ACTA2, and NG2) markers using flow cytometry. Left: representative 2D scatterplots; Right: summarized results with mean and SEM from 3 independent biological repeats.

(E) F-actin assembly. Left: representative immunofluorescence images from FGF2, C6-79C_mb7 and mb7 + FGF2-derived cells (PDGFR-B, perivascular cells; PHAL, F-actin). Scale bars: 100 μm. Right: summarized per-cell phalloidin (PHAL) intensity from 3 independent biological repeats (7 randomly chosen field of views from each).

(F) 2D network formation. Normalized count of nodes, segments, and meshes after 24 h, summarized from 3 independent biological repeats (5 randomly chosen fields of view from each).

(G) Cell migration. Percentage closure of inflicted scratch area after 6 and 24 h, summarized from 3 independent biological repeats (3 randomly chosen field of views from each).

(H) LDL uptake. Representative flow cytometry of fluorescently labeled LDL uptake by cells generated using FGF2, C6-79C_mb7, and mb7 + FGF2 after 4 h of treatment. Mean and SEM are reported from 3 independent biological repeats.

We used flow cytometry with endothelial and perivascular cell surface markers to further characterize the cells harvested at day 14 of differentiation. Populations derived using FGF2 or C6-79C_mb7 were similar in composition, consisting primarily of endothelial cells (VE-cadherin+ cells: 81.2% and 69.9%, respectively; CD31+ cells: 70.1% and 87.2%, respectively; CLND5+ cells: 34.9% and 41.2%, respectively), whereas cells derived using mb7 in combination with FGF2 were overwhelmingly perivascular in identity (PDGFR-B+ cells: 76.2%; NG2+ cells: 33.9%; ACTA2+ cells: 16.2%) (Figure 5D). These results agree with the trend seen in the transcriptomic data—signaling of FGFRs through their c-isoform is critical for the development of endothelial cells, while b-isoform-specific signaling instead promotes the perivascular lineage.

Perivascular cells are contractile cells that are known to play a role in capillary blood flow regulation through the assembly of F-actin bundles[52,53]; we characterized our cell populations by measuring intracellular actin (using fluorescently labeled phalloidin) at day 14 of differentiation. Cells derived using mb7 + FGF2 exhibited ~4-fold increase in F-actin assembly over cells derived using FGF2 or C6-79C_mb7 (Figure 5E) owing to the robust formation of stress fibers in these perivascular cells. To characterize the functional maturity of the endothelial populations, we used tube formation,[54] cell migration,[55,56] LDL uptake,[57] and cytokine challenge[58] assays. The capacity to assemble into capillary-like tubules is a hallmark phenotype of endothelial cells,[59] and the cells derived via FGFR c-isoform activation demonstrated a robust 2D network formation capacity (measured by numbers of nodes, segments, and meshes in a tube formation assay) (Figures 5F and S24A). In addition, these cells readily migrated, completely sealing an inflicted scratch within 24 h (Figures 5G and S24B). Low-density lipoprotein (LDL) uptake is a critical process observed in endothelial cells to acquire cholesterol,[60] and we found that endothelial cells derived using FGF2 and C6-79C_mb7 (but not mb7 + FGF2) exhibited high and comparable levels of receptor-mediated uptake of fluorophore-labeled LDL (Figure 5H). Finally, endothelial cells are known to upregulate vascular cell adhesion molecule 1 (VCAM-1) (for adhesion and trans-endothelial migration of leukocytes) in response to inflammatory cytokines,[61,62] and we observed that endothelial cells derived using FGF2 and C6-79C_mb7 (but not mb7 + FGF2), upon exposure to tumor necrosis factor alpha (TNF-α), displayed a significant increase in VCAM-1 expression (Figure 5I). These results suggest that the endothelial cells generated via c-isoform activity are functional and mature, with increased endothelial functionality compared with cells derived using the FGFR c-isoform antagonist (mb7 + FGF2), which exhibit more of a perivascular identity.

Arterial versus venous endothelial cell fate specification

Sub-clustering of the day-14 endothelial expression data suggested that arterial and venous endothelial cells emerged in different ratios with the different treatments.[63] In order to characterize these sub-populations, we compared our endothelial expression data with a previously published RNA-seq dataset from arterial and venous endothelial cells generated from human pluripotent stem cells.[64] We used the genes identified as differentially expressed in arterial and venous cells in this dataset to assign an arteriovenous specificity score for each cell in our endothelial dataset, and classified cells that scored above the median specificity score as arterial, and cells below the score as venous. We found that endothelial cells generated with or without added FGF2 primarily adopted the venous cell fate (68% or 86% venous, respectively), while C6-79C_mb7 induced a strong bias toward an arterial-like endothelial cell fate (64% arterial-like) (Figure 6A).

We hypothesized that the clear emergence of endothelial subtypes at the protein level would require further maturation of the iPSC-derived endothelial cells. To this end, we adapted a previously described protocol for creating self-organizing 3D blood vessel organoids (BVOs) from pluripotent stem cells[65] (Figure S25A). These organoids contain the major cell types (endothelial and perivascular cells) that assemble into capillary-like networks, and, importantly, these organoids can be grown and matured for more than 60 days in culture. We replaced FGF2 in the protocol with an equivalent concentration of C6-79C_mb7 between days 5 and 13, which mimics days 2–5 in 2D culture in respect of the emergence of mesodermal intermediates and promotion of vascular lineages.[66] Organoids were harvested at day 37 and stained for VE-cadherin (to observe the formation of vascular networks) and EFNB2 (to detect arterial-like endothelial cells). Cells in organoids derived using C6-79C_mb7 exhibited significantly higher average expression of EFNB2 (Figures 6B and S25B), suggesting that c-isoform activation of FGFRs biases endothelial cells toward an arterial fate following maturation.

BVOs can form stable vascular networks upon transplantation into immunodeficient mice.[65,66] To investigate whether organoids generated using C6-79C_mb7 could replicate this phenotype, we transplanted day 21 C6-79C_mb7-derived and FGF2-derived organoids under the kidney capsule of immunodeficient mice and harvested tissues after 3 weeks. Immunohistochemical analysis revealed the emergence of human vascular endothelial (hVE-cadherin+ or hCD31+) networks with outgrowths into the surrounding stroma that formed connections with mouse (mCD31+) vascular cells (Figures 6C and S26). These results highlight the potential of designed proteins as tailored agonists for differentiation of cells into highly specific lineages.

DISCUSSION

The extensible star-shaped oligomers designed in this work considerably expand the tools available for clustering cell surface receptors and other targets with different valencies and geometries. The designed scaffolds are highly expressed in *E. coli* and the spacing of attached binding domains can be systematically varied simply by adding or deleting the modular repeat

---

(I) Cytokine challenge assay. Representative immunofluorescence images of cells treated with TNF-α (10 ng/mL) for 24 h, summarized from 3 independent biological repeats (5 randomly chosen fields from each) (VCAM1, vascular cell adhesion molecule 1). Scale bars: 100 μm. *$p < 0.05$, **$p < 0.01$, Student's two-tailed t test.
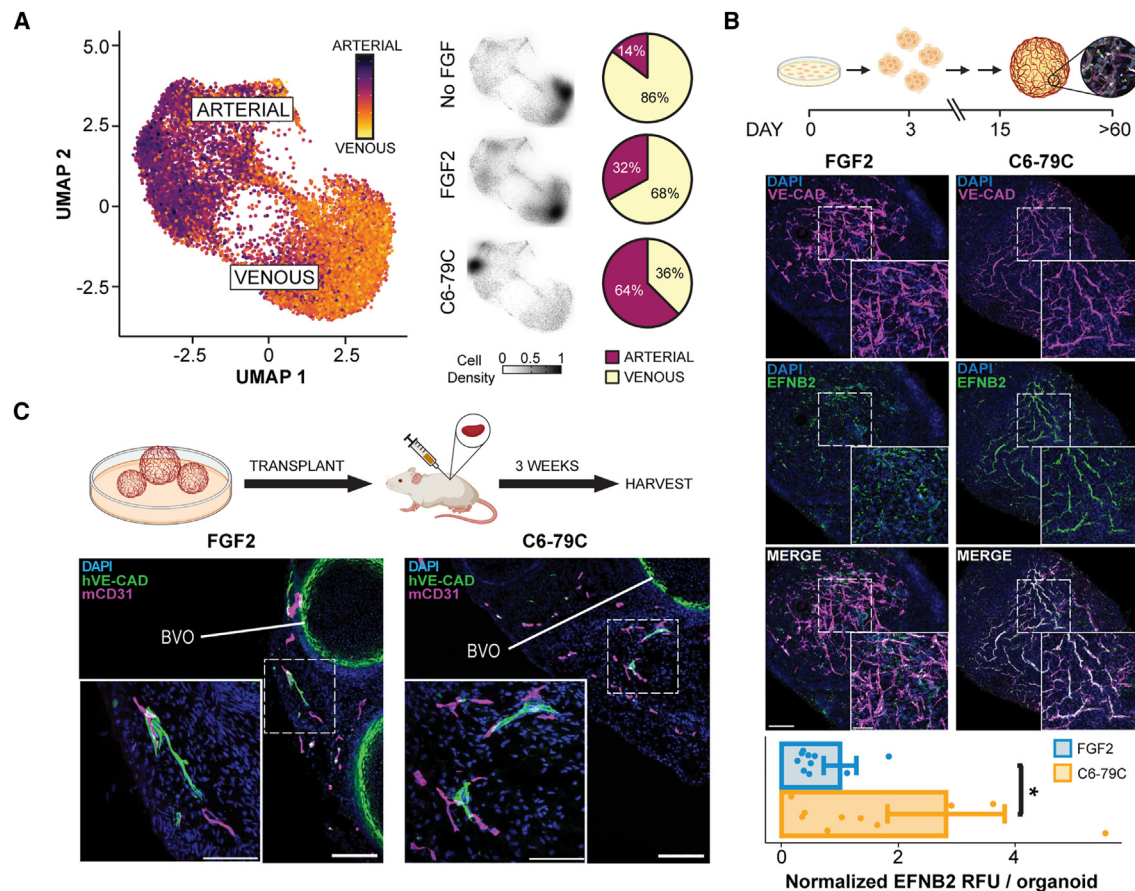See also Figures S23 and S24 and Table S7.

Cell
Article

Figure 6. Control over endothelial subtype fate via isoform-specific agonism
(A) Left: UMAP embeddings of sub-clustered endothelial cells, colored by arteriovenous cell specificity. Middle: density plots showing specific endothelial subtype populations enriched by the individual treatments. Right: proportion of arterial or venous endothelial cells generated at day 14 following treatment with No FGF, FGF2, or C6-79C_mb7.
(B) Top: representative immunofluorescence images of blood vessel organoids (BVOs) generated using FGF2 or C6-79C_mb7. Vascular networks are marked with VE-cadherin and arterial-like endothelial cells are marked with EFNB2. Scale bars: 200 μm (whole) and 50 μm (inset). Bottom: per-organoid quantification of EFNB2, summarizing 10 independently generated organoids from each treatment.
(C) Immunohistochemical characterization of BVOs transplanted under the mouse kidney capsule. Scale bars: 200 μm (whole) and 100 μm (inset). *$p < 0.05$, Student's two-tailed t test.
See also Figures S25 and S26.

units. C8-71 and its extensions are the first designed scaffolds offering both a defined octameric symmetry and a stepwise variation in diameter through repeat units. The highest success rate was achieved with the DHR71 building block, perhaps because the design model (used in the docking protocol to avoid issues of missing terminal residues or imperfect repeat unit symmetry in the crystal structure) was closer to the crystal structure (0.67 Å RMSD),[25] leading to greater accuracy of the oligomer computational models.

FGFR homodimerizes upon FGF binding, and hence attention has focused on activation of the FGFR pathway by receptor homodimerization and heparin-based oligomerization.[67] The multivalent binders stimulate FGFR activation by dimerizing FGFRs or by driving higher order assemblies. We observed pathway activation by C2, C4, C6, and C8 FGFR engaging ligands, which varied when the geometry of presentation was tuned by varying the

length of the radially extending arms. The C4 extension series revealed a strong distance dependence for activation: mb7 templated 53 Å apart showed strong pERK signaling, whereas the larger constructs with extension lengths of 76 and 96 Å did not signal, consistent with the FGF2-FGFR1 dimer complex structure (PDB: 1FQ9)[68] in which the membrane proximal termini are 48 Å apart. Direct measurement of FGFR diffusion in the membrane (Figure S17) and of the oligomerization state of the receptor in the membrane (Figures 4D and 4E) suggest that synthetic ligands drive FGFR clustering.

Commercially available naturally occurring signaling molecules (such as FGF2) often have pleiotropic effects and it can be difficult to use these to promote differentiation of highly specific cell subpopulations; small molecule treatments can have similar limitations. Our designed proteins not only recapitulate classical aspects of FGF signaling but also have a number of
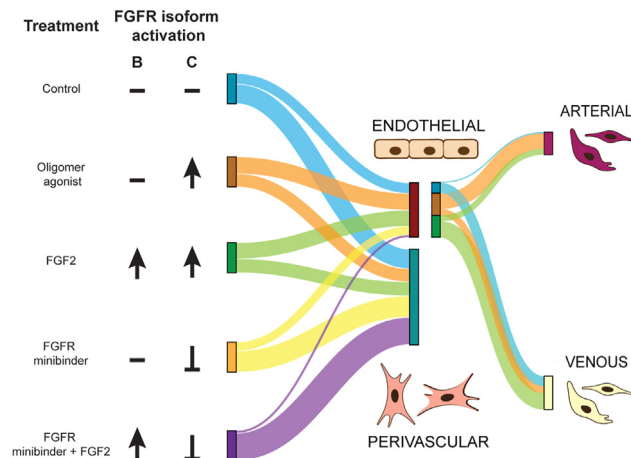
CellPress
OPEN ACCESS

Figure 7. Control over vascular differentiation

At the first bifurcation, the designs enable selective formation of endothelial or perivascular cells, and in subsequent endothelial cell differentiation, synthetic agonist treatments bias toward arterial fate.

distinct advantages in sustained signaling, promotion of vascular differentiation, and ease of production. Likely because of the slow off rate of mb7 for FGFR, and the avid binding of the multivalent constructs, the calcium transients elicited by our synthetic agonists have longer duration than those elicited by FGF. The specificity of mb7 for the c-isoform[21] enables specific activation of signaling through the c-isoform receptor, while addition of mb7 to FGF enables activation of signaling exclusively through the b-isoform. These and perhaps other subtle differences in proximal signaling result in distinct outcomes at multiple developmental stages in vascular differentiation. Our designed scaffolds provide a means to control the prevalence of endothelial or perivascular cells by taking advantage of the capability to activate signaling through just the b- or just the c-receptor isoforms (Figure 7). In subsequent endothelial cell differentiation, C6-79C_mb7 promotes the arterial cell fate. Although the tissue distributions of different FGFR splice forms have been extensively characterized,[24] our work goes beyond previous studies by delineating their functional roles in vascular endothelial differentiation. Our splice-variant-specific designs can promote either the endothelial cell or perivascular fate, and can elicit specific subtypes of vascular endothelial cells, and should be useful for both probing biological mechanisms and therapeutic applications.

Limitations of the study

Here, we used flexible fusion of the FGFR-binding domain to pre-existing oligomers; rigid fusion to custom-generated oligomers using methods such as RFDiffusion[18] could provide tighter control of receptor architecture and fine-tuning of signaling outcome.[10] On the biology side, we were unable to carry out genetic knockouts of FGFR1/2c to further test the role of this variant in the developing iPSC-derived endothelium because FGFR1/2c appears to be essential earlier during human pluripotency. Designed agonists and antagonists with receptor-isoform-dependent specificity provide an approach for probing the roles of

different isoforms in developmental bifurcations when genetic knockouts are not feasible due to early essentiality. The designed-oligomer-based approach described here provides a versatile way in which to promote receptor clustering and shape pathway activation with multiple levels of control compared with the native signaling molecules: the receptor-binding domains can have higher receptor subtype specificity, the on and off rates for receptor subunits can be tuned, and the valency and geometry of receptor engagement can be systematically varied. We envision that such customized synthetic agonists will have broad applications in both *ex vivo* and *in vivo* control of cellular differentiation.

STAR★METHODS

Detailed methods are provided in the online version of this paper and include the following:

- KEY RESOURCES TABLE
- RESOURCE AVAILABILITY
  - Lead contact
  - Materials availability
  - Data and code availability
- EXPERIMENTAL MODEL AND STUDY PARTICIPANT DETAILS
  - Cell lines
  - Animals
- METHOD DETAILS
  - Scaffold selection and cyclic docking
  - 5 helix concave scaffold generation
  - Repeat extension script
  - Expression and purification
  - Low-endotoxin protein production
  - Size exclusion chromatography with multi-angle light scattering
  - Negative stain EM grid preparation, data collection, and data processing
  - Small-angle X-ray scattering
  - Cryo-EM grid preparation and data collection
  - Processing of 200 kV cryo-EM screening datasets (C4-71 extensions, C6-71 and extensions, C8-71 extensions)
  - Processing of 300 kV cryo-EM datasets (C4-71, C4-81, C6-79, C8-71)
  - C6-79 and C8-71 model building and refinement
  - Cell culture
  - Treatment and protein isolation for Western blot and proteomics
  - Western blotting
  - Calcium release assay
  - Phosphoflow assay
  - Biolayer interferometry (BLI) assay
  - TIRF microscopy
  - Single-particle tracking
  - Transcriptomics on HUVEC endothelial cells
  - Immunostaining of differentiated iPSCs
  - *In vitro* differentiation of endothelial cells
  - Sample preparation for proteomics analysis
  - Mass spectra data analysis
  - Flow cytometry
  - Cell migration assay
  - Tube formation assay
  - LDL uptake assay
  - Cytokine challenge assay
  - F-actin assembly
  - Blood vessel organoids
  - Immunostaining of blood vessel organoids
  - *In vivo* injections of blood vessel organoids
- QUANTIFICATION AND STATISTICAL ANALYSIS

![CellPress OPEN ACCESS logo]

Cell
Article

AUTHOR CONTRIBUTIONS

N.I.E. and D.B. conceived the project. A.P. and H.R.-B. conceived analyzing the designed proteins in endothelial differentiation. N.I.E. and A.E. designed oligomeric constructs. W.Y., B.C., and D.R.H. designed building blocks for oligomers. N.I.E., T.S., A.F., Z.L., L.C., and M.M. characterized oligomers. F.P. developed the script for oligomer extension. R.L.R., G.B., D.C.E., and N.I.E. performed EM analysis of the designed constructs. N.B. performed cyclic docking of the oligomers. A.P., T.S., S.A., M.G., and D.D.E. performed cell assays. A.P., T.V., S.M., L.B., C.E.M., B.S.F., H.R-B., and Y.Z. designed, performed, or supervised animal experiments. A.P., D.D.E., and H.R-B. performed or supervised organoid assays. C.L. and D.K.S. performed proteomics experiments. L.C. and B.C. developed the minibinder. N.I.E., T.S., P.H., A.M., and S.G. purified the endotoxin-free protein. S.L. provided L6-R1c and L6-R1b cells. A.P. and S.R.S. performed the transcriptomics study. D.B., L.S., J.S., C.T., B.N., J.S., and H.R.-B. supervised the study. N.I.E., T.S., A.P., R.L.R., H.R.-B., and D.B. wrote the manuscript with input from all authors.

REFERENCES

1. Garcia-Parajo, M.F., Cambi, A., Torreno-Pina, J.A., Thompson, N., and Jacobson, K. (2014). Nanoclustering as a dominant feature of plasma membrane organization. J. Cell Sci. *127*, 4995–5005. https://doi.org/10.1242/jcs.146340.

2. Wu, H. (2013). Higher-order assemblies in a new paradigm of signal transduction. Cell *153*, 287–292. https://doi.org/10.1016/J.CELL.2013.03.013.

3. Mayer, B.J., and Yu, J. (2018). Protein Clusters in Phosphotyrosine Signal Transduction. J. Mol. Biol. *430*, 4547–4556. https://doi.org/10.1016/J.JMB.2018.05.040.

4. Westerfield, J.M., and Barrera, F.N. (2020). Membrane receptor activation mechanisms and transmembrane peptide tools to elucidate them. J. Biol. Chem. *295*, 1792–1814. https://doi.org/10.1074/jbc.REV119.009457.

5. Zhang, K., Gao, H., Deng, R., and Li, J. (2019). Emerging Applications of Nanotechnology for Controlling Cell-Surface Receptor Clustering. Angew. Chem. Int. Ed. Engl. *58*, 4790–4799. https://doi.org/10.1002/anie.201809006.

6. Porębska, N., Ciura, K., Chorążewska, A., Zakrzewska, M., Otlewski, J., and Opaliński, Ł. (2023). Multivalent protein-drug conjugates - An emerging strategy for the upgraded precision and efficiency of drug delivery to cancer cells. Biotechnol. Adv. *67*, 108213. https://doi.org/10.1016/j.biotechadv.2023.108213.

7. Zhao, Y.T., Fallas, J.A., Saini, S., Ueda, G., Somasundaram, L., Zhou, Z., Xavier Raj, I., Xu, C., Carter, L., Wrenn, S., et al. (2021). F-domain valency determines outcome of signaling through the angiopoietin pathway. EMBO Rep. *22*, e53471. https://doi.org/10.15252/embr.202153471.

8. Divine, R., Dang, H.V., Ueda, G., Fallas, J.A., Vulovic, I., Sheffler, W., Saini, S., Zhao, Y.T., Raj, I.X., Morawski, P.A., et al. (2021). Designed proteins assemble antibodies into modular nanocages. Science *372*, eabd9994. https://doi.org/10.1126/science.abd9994.

9. Ben-Sasson, A.J., Watson, J.L., Sheffler, W., Johnson, M.C., Bittleston, A., Somasundaram, L., Decarreau, J., Jiao, F., Chen, J., Mela, I., et al. (2021). Design of biologically active binary protein 2D materials. Nature *589*, 468–473. https://doi.org/10.1038/s41586-020-03120-8.

10. Mohan, K., Ueda, G., Kim, A.R., Jude, K.M., Fallas, J.A., Guo, Y., Hafer, M., Miao, Y., Saxton, R.A., Piehler, J., et al. (2019). Topological control of cytokine receptor signaling induces differential effects in hematopoiesis. Science *364*, eaav7532. https://doi.org/10.1126/science.aav7532.

11. Moraga, I., Spangler, J.B., Mendoza, J.L., Gakovic, M., Wehrman, T.S., Krutzik, P., and Garcia, K.C. (2017). Synthekines are surrogate cytokine

and growth factor agonists that compel signaling through non-natural receptor dimers. eLife 6, e22882. https://doi.org/10.7554/eLife.22882.

12. Yang, C., Sesterhenn, F., Bonet, J., van Aalen, E.A., Scheller, L., Abriata, L.A., Cramer, J.T., Wen, X., Rosset, S., Georgeon, S., et al. (2021). Bottom-up de novo design of functional proteins with complex structural features. Nat. Chem. Biol. 17, 492–500. https://doi.org/10.1038/s41589-020-00699-x.

13. Shaw, A., Lundin, V., Petrova, E., Fördős, F., Benson, E., Al-Amin, A., Herland, A., Blokzijl, A., Högberg, B., and Teixeira, A.I. (2014). Spatial control of membrane receptor function using ligand nanocalipers. Nat. Methods 11, 841–846. https://doi.org/10.1038/nmeth.3025.

14. Taga, T., and Kishimoto, T. (1997). Gp130 and the interleukin-6 family of cytokines. Annu. Rev. Immunol. 15, 797–819. https://doi.org/10.1146/annurev.immunol.15.1.797.

15. Martinez-Moczygemba, M., and Huston, D.P. (2003). Biology of common β receptor–signaling cytokines: il-3, IL-5, and GM-CSF. J. Allergy Clin. Immunol. 112, 653–665. https://doi.org/10.1016/S0091.

16. Boulanger, M.J., Chow, D.C., Brevnova, E.E., and Garcia, K.C. (2003). Hexameric structure and assembly of the interleukin-6/IL-6 alpha-receptor/gp130 complex. Science 300, 2101–2104. https://doi.org/10.1126/science.1083901.

17. Gerben, S.R., Borst, A.J., Hicks, D.R., Moczygemba, I., Feldman, D., Coventry, B., Yang, W., Bera, A.K., Miranda, M., Kang, A., et al. (2023). Design of Diverse Asymmetric Pockets in De Novo Homo-oligomeric Proteins. Biochemistry 62, 358–368. https://doi.org/10.1021/acs.biochem.2c00497.

18. Watson, J.L., Juergens, D., Bennett, N.R., Trippe, B.L., Yim, J., Eisenach, H.E., Ahern, W., Borst, A.J., Ragotte, R.J., Milles, L.F., et al. (2023). De novo design of protein structure and function with RFdiffusion. Nature 620, 1089–1100. https://doi.org/10.1038/s41586-023-06415-8.

19. Wicky, B.I.M., Milles, L.F., Courbet, A., Ragotte, R.J., Dauparas, J., Kinfu, E., Tipps, S., Kibler, R.D., Baek, M., DiMaio, F., et al. (2022). Hallucinating symmetric protein assemblies. Science 378, 56–61. https://doi.org/10.1126/science.add1964.

20. Fallas, J.A., Ueda, G., Sheffler, W., Nguyen, V., McNamara, D.E., Sankaran, B., Pereira, J.H., Parmeggiani, F., Brunette, T.J., Cascio, D., et al. (2017). Computational design of self-assembling cyclic protein homo-oligomers. Nat. Chem. 9, 353–360. https://doi.org/10.1038/NCHEM.2673.

21. Park, J.S., Choi, J., Cao, L., Mohanty, J., Suzuki, Y., Park, A., Baker, D., Schlessinger, J., and Lee, S. (2022). Isoform-specific inhibition of FGFR signaling achieved by a de-novo-designed mini-protein. Cell Rep. 41, 111545. https://doi.org/10.1016/j.celrep.2022.111545.

22. Holzmann, K., Grunt, T., Heinzle, C., Sampl, S., Steinhoff, H., Reichmann, N., Kleiter, M., Hauck, M., and Marian, B. (2012). Alternative Splicing of Fibroblast Growth Factor Receptor IgIII Loops in Cancer. J. Nucleic Acids 2012, 950508. https://doi.org/10.1155/2012/950508.

23. Yeh, B.K., Igarashi, M., Eliseenkova, A.V., Plotnikov, A.N., Sher, I., Ron, D., Aaronson, S.A., and Mohammadi, M. (2003). Structural basis by which alternative splicing confers specificity in fibroblast growth factor receptors. Proc. Natl. Acad. Sci. USA 100, 2266–2271. https://doi.org/10.1073/pnas.0436500100.

24. Turner, N., and Grose, R. (2010). Fibroblast growth factor signalling: from development to cancer. Nat. Rev. Cancer 10, 116–129. https://doi.org/10.1038/nrc2780.

25. Brunette, T.J., Parmeggiani, F., Huang, P.-S.S., Bhabha, G., Ekiert, D.C., Tsutakawa, S.E., Hura, G.L., Tainer, J.A., and Baker, D. (2015). Exploring the repeat protein universe through computational protein design. Nature 528, 580–584. https://doi.org/10.1038/nature16162.

26. Brunette, T.J., Bick, M.J., Hansen, J.M., Chow, C.M., Kollman, J.M., and Baker, D. (2020). Modular repeat protein sculpting using rigid helical junctions. Proc. Natl. Acad. Sci. USA 117, 8870–8875. https://doi.org/10.1073/pnas.1908768117.

27. Sheffler, W., Yang, E.C., Dowling, Q., Hsia, Y., Fries, C.N., Stanislaw, J., Langowski, M., Brandys, M., Khmelinskaia, A., King, N.P., et al. Fast and versatile sequence-independent protein docking for nanomaterials design using RPXDock. PLoS Comput. Biol. 19, e1010680. 10.1371/journal.pcbi.1010680.

28. Coventry, B., and Baker, D. (2021). Protein sequence optimization with a pairwise decomposable penalty for buried unsatisfied hydrogen bonds. PLoS Comput. Biol. 17, e1008061. https://doi.org/10.1371/journal.pcbi.1008061.

29. Boyken, S.E., Chen, Z., Groves, B., Langan, R.A., Oberdorfer, G., Ford, A., Gilmore, J.M., Xu, C., DiMaio, F., Pereira, J.H., et al. (2016). De novo design of protein homo-oligomers with modular hydrogen-bond network-mediated specificity. Science 352, 680–687. https://doi.org/10.1126/science.aad8865.

30. Maguire, J.B., Haddox, H.K., Strickland, D., Halabiya, S.F., Coventry, B., Griffin, J.R., Pulavarti, S.V.S.R.K., Cummins, M., Thieker, D.F., Klavins, E., et al. (2021). Perturbing the energy landscape for improved packing during computational protein design. Proteins 89, 436–449. https://doi.org/10.1002/prot.26030.

31. Yang, W., Hicks, D.R., Ghosh, A., Schwartze, T.A., Coventry, B., Goreshnik, I., Allen, A., Halabiya, S.F., Kim, C.J., Hinck, C.S., et al. (2024). Design of High Affinity Binders to Convex Protein Target Sites. Preprint at bioRxiv. https://doi.org/10.1101/2024.05.01.592114.

32. Dyer, K.N., Hammel, M., Rambo, R.P., Tsutakawa, S.E., Rodic, I., Classen, S., Tainer, J.A., and Hura, G.L. (2014). High-throughput SAXS for the characterization of biomolecules in solution: a practical approach. Methods Mol. Biol. 1091, 245–258. https://doi.org/10.1007/978-1-62703-691-7_12.

33. Classen, S., Hura, G.L., Holton, J.M., Rambo, R.P., Rodic, I., McGuire, P.J., Dyer, K., Hammel, M., Meigs, G., Frankel, K.A., et al. (2013). Implementation and performance of SIBYLS: a dual endstation small-angle X-ray scattering and macromolecular crystallography beamline at the Advanced Light Source. J. Appl. Crystallogr. 46, 1–13. https://doi.org/10.1107/S0021889812048698.

34. Putnam, C.D., Hammel, M., Hura, G.L., and Tainer, J.A. (2007). X-ray solution scattering (SAXS) combined with crystallography and computation: defining accurate macromolecular structures, conformations and assemblies in solution. Q. Rev. Biophys. 40, 191–285. https://doi.org/10.1017/S0033583507004635.

35. Lemmon, M.A., and Schlessinger, J. (2010). Cell signaling by receptor tyrosine kinases. Cell 141, 1117–1134. https://doi.org/10.1016/j.cell.2010.06.011.

36. Cao, L., Coventry, B., Goreshnik, I., Huang, B., Sheffler, W., Park, J.S., Jude, K.M., Marković, I., Kadam, R.U., Verschueren, K.H.G., et al. (2022). Design of protein-binding proteins from the target structure alone. Nature 605, 551–560. https://doi.org/10.1038/s41586-022-04654-9.

37. Ornitz, D.M., and Itoh, N. (2015). The Fibroblast Growth Factor signaling pathway. Wiley Interdiscip. Rev. Dev. Biol. 4, 215–266. https://doi.org/10.1002/wdev.176.

38. Ferguson, H.R., Smith, M.P., and Francavilla, C. (2021). Fibroblast Growth Factor Receptors (FGFRs) and Noncanonical Partners in Cancer Signaling. Cells 10, 1–35. https://doi.org/10.3390/cells10051201.

39. Wu, S., Jin, L., Vence, L., and Radvanyi, L.G. (2010). Development and application of "phosphoflow" as a tool for immunomonitoring. Expert Rev. Vaccines 9, 631–643. https://doi.org/10.1586/erv.10.59.

40. Los, G.V., Encell, L.P., McDougall, M.G., Hartzell, D.D., Karassina, N., Zimprich, C., Wood, M.G., Learish, R., Ohana, R.F., Urh, M., et al. (2008). HaloTag: A novel protein labeling technology for cell imaging and protein analysis. ACS Chem. Biol. 3, 373–382. https://doi.org/10.1021/cb800025k.

41. Jaqaman, K., Kuwata, H., Touret, N., Collins, R., Trimble, W.S., Danuser, G., and Grinstein, S. (2011). Cytoskeletal control of CD36 diffusion promotes its receptor and signaling function. Cell 146, 593–606. https://doi.org/10.1016/j.cell.2011.06.049.

42. Lee, S.-H., Shin, J.Y., Lee, A., and Bustamante, C. (2012). Counting single photoactivatable fluorescent molecules by photoactivated localization microscopy (PALM). Proc. Natl. Acad. Sci. USA 109, 17436–17441. https://doi.org/10.1073/pnas.1215175109.

43. Gong, S.-G. (2014). Isoforms of receptors of fibroblast growth factors. J. Cell. Physiol. 229, 1887–1895. https://doi.org/10.1002/jcp.24649.

44. Kumar, V., Goutam, R.S., Park, S., Lee, U., and Kim, J. (2021). Functional Roles of FGF Signaling in Early Development of Vertebrate Embryos. Cells 10, 2148. https://doi.org/10.3390/cells10082148.

45. Dorey, K., and Amaya, E. (2010). FGF signalling: diverse roles during early vertebrate embryogenesis. Development 137, 3731–3742. https://doi.org/10.1242/dev.037689.

46. Yu, P., Wilhelm, K., Dubrac, A., Tung, J.K., Alves, T.C., Fang, J.S., Xie, Y., Zhu, J., Chen, Z., De Smet, F., et al. (2017). FGF-dependent metabolic control of vascular development. Nature 545, 224–228. https://doi.org/10.1038/nature22322.

47. Javerzat, S., Auguste, P., and Bikfalvi, A. (2002). The role of fibroblast growth factors in vascular development. Trends Mol. Med. 8, 483–489. https://doi.org/10.1016/S1471-4914(02)02394-8.

48. Di Matteo, A., Belloni, E., Pradella, D., Cappelletto, A., Volf, N., Zacchigna, S., and Ghigna, C. (2020). Alternative splicing in endothelial cells: novel therapeutic opportunities in cancer angiogenesis. J. Exp. Clin. Cancer Res. 39, 275. https://doi.org/10.1186/s13046-020-01753-1.

49. Palpant, N.J., Pabon, L., Friedman, C.E., Roberts, M., Hadland, B., Zaunbrecher, R.J., Bernstein, I., Zheng, Y., and Murry, C.E. (2017). Generating high-purity cardiac and endothelial derivatives from patterned mesoderm using human pluripotent stem cells. Nat. Protoc. 12, 15–31. https://doi.org/10.1038/nprot.2016.153.

50. Ornitz, D.M., Xu, J., Colvin, J.S., McEwen, D.G., MacArthur, C.A., Coulier, F., Gao, G., and Goldfarb, M. (1996). Receptor Specificity of the Fibroblast Growth Factor Family. J. Biol. Chem. 271, 15292–15297. https://doi.org/10.1074/jbc.271.25.15292.

51. Cao, J., Spielmann, M., Qiu, X., Huang, X., Ibrahim, D.M., Hill, A.J., Zhang, F., Mundlos, S., Christiansen, L., Steemers, F.J., et al. (2019). The single-cell transcriptional landscape of mammalian organogenesis. Nature 566, 496–502. https://doi.org/10.1038/s41586-019-0969-x.

52. Kureli, G., Yilmaz-Ozcan, S., Erdener, S.E., Donmez-Demir, B., Yemisci, M., Karatas, H., and Dalkara, T. (2020). F-actin polymerization contributes to pericyte contractility in retinal capillaries. Exp. Neurol. 332, 113392. https://doi.org/10.1016/j.expneurol.2020.113392.

53. Erdener, Ş.E., Küreli, G., and Dalkara, T. (2022). Contractile apparatus in CNS capillary pericytes. Neurophotonics 9, 021904. https://doi.org/10.1117/1.NPh.9.2.021904.

54. Kubota, Y., Kleinman, H.K., Martin, G.R., and Lawley, T.J. (1988). Role of laminin and basement membrane in the morphological differentiation of human endothelial cells into capillary-like structures. J. Cell Biol. 107, 1589–1598. https://doi.org/10.1083/jcb.107.4.1589.

55. Liang, C.-C., Park, A.Y., and Guan, J.-L. (2007). In vitro scratch assay: a convenient and inexpensive method for analysis of cell migration in vitro. Nat. Protoc. 2, 329–333. https://doi.org/10.1038/nprot.2007.30.

56. Chim, S.M., Qin, A., Tickner, J., Pavlos, N., Davey, T., Wang, H., Guo, Y., Zheng, M.H., and Xu, J. (2011). EGFL6 promotes endothelial cell migration and angiogenesis through the activation of extracellular signal-regulated kinase. J. Biol. Chem. 286, 22035–22046. https://doi.org/10.1074/jbc.M110.187633.

57. Voyta, J.C., Via, D.P., Butterfield, C.E., and Zetter, B.R. (1984). Identification and isolation of endothelial cells based on their increased uptake of acetylated-low density lipoprotein. J. Cell Biol. 99, 2034–2040. https://doi.org/10.1083/jcb.99.6.2034.

58. Amersfoort, J., Eelen, G., and Carmeliet, P. (2022). Immunomodulation by endothelial cells - partnering up with the immune system? Nat. Rev. Immunol. 22, 576–588. https://doi.org/10.1038/s41577-022-00694-4.

59. Arnaoutova, I., and Kleinman, H.K. (2010). In vitro angiogenesis: endothelial cell tube formation on gelled basement membrane extract. Nat. Protoc. 5, 628–635. https://doi.org/10.1038/nprot.2010.6.

60. Zhang, X., Sessa, W.C., and Fernández-Hernando, C. (2018). Endothelial Transcytosis of Lipoproteins in Atherosclerosis. Front. Cardiovasc. Med. 5, 130. https://doi.org/10.3389/fcvm.2018.00130.

61. Chiu, J.-J., Lee, P.-L., Chen, C.-N., Lee, C.-I., Chang, S.-F., Chen, L.-J., Lien, S.-C., Ko, Y.-C., Usami, S., and Chien, S. (2004). Shear stress increases ICAM-1 and decreases VCAM-1 and E-selectin expressions induced by tumor necrosis factor-[alpha] in endothelial cells. Arterioscler. Thromb. Vasc. Biol. 24, 73–79. https://doi.org/10.1161/01.ATV.0000106321.63667.24.

62. Singh, R.J.R., Mason, J.C., Lidington, E.A., Edwards, D.R., Nuttall, R.K., Khokha, R., Knauper, V., Murphy, G., and Gavrilovic, J. (2005). Cytokine stimulated vascular cell adhesion molecule-1 (VCAM-1) ectodomain release is regulated by TIMP-3. Cardiovasc. Res. 67, 39–49. https://doi.org/10.1016/j.cardiores.2005.02.020.

63. Potente, M., and Mäkinen, T. (2017). Vascular heterogeneity and specialization in development and disease. Nat. Rev. Mol. Cell Biol. 18, 477–494. https://doi.org/10.1038/nrm.2017.36.

64. Ang, L.T., Nguyen, A.T., Liu, K.J., Chen, A., Xiong, X., Curtis, M., Martin, R.M., Raftry, B.C., Ng, C.Y., Vogel, U., et al. (2022). Generating human artery and vein cells from pluripotent stem cells highlights the arterial tropism of Nipah and Hendra viruses. Cell 185, 2523–2541.e30. https://doi.org/10.1016/j.cell.2022.05.024.

65. Wimmer, R.A., Leopoldi, A., Aichinger, M., Wick, N., Hantusch, B., Novatchkova, M., Taubenschmid, J., Hämmerle, M., Esk, C., Bagley, J.A., et al. (2019). Human blood vessel organoids as a model of diabetic vasculopathy. Nature 565, 505–510. https://doi.org/10.1038/s41586-018-0858-8.

66. Nikolova, M.T., He, Z., Wimmer, R.A., Seimiya, M., Nikoloff, J.M., Penninger, J.M., Gray Camp, J., and Treutlein, B. (2022). Fate and state transitions during human blood vessel organoid development. Preprint at bioRxiv. https://doi.org/10.1101/2022.03.23.485329.

67. Spivak-Kroizman, T., Lemmon, M.A., Dikic, I., Ladbury, J.E., Pinchasi, D., Huang, J., Jaye, M., Crumley, G., Schlessinger, J., and Lax, I. (1994). Heparin-induced oligomerization of FGF molecules is responsible for FGF receptor dimerization, activation, and cell proliferation. Cell 79, 1015–1024. https://doi.org/10.1016/0092-8674(94)90032-9.

68. Schlessinger, J., Plotnikov, A.N., Ibrahimi, O.A., Eliseenkova, A.V., Yeh, B.K., Yayon, A., Linhardt, R.J., and Mohammadi, M. (2000). Crystal structure of a ternary FGF-FGFR-heparin complex reveals a dual role for heparin in FGFR binding and dimerization. Mol. Cell 6, 743–750. https://doi.org/10.1016/s1097-2765(00)00073-3.

69. Leman, J.K., Weitzner, B.D., Lewis, S.M., Adolf-Bryfogle, J., Alam, N., Alford, R.F., Aprahamian, M., Baker, D., Barlow, K.A., Barth, P., et al. (2020). Macromolecular modeling and design in Rosetta: recent methods and frameworks. Nat. Methods 17, 665–680. https://doi.org/10.1038/s41592-020-0848-2.

70. Zivanov, J., Nakane, T., Forsberg, B.O., Kimanius, D., Hagen, W.J., Lindahl, E., and Scheres, S.H. (2018). New tools for automated high-resolution cryo-EM structure determination in RELION-3. eLife 7, e42166. https://doi.org/10.7554/eLife.42166.

71. Punjani, A., Rubinstein, J.L., Fleet, D.J., and Brubaker, M.A. (2017). cryoSPARC: algorithms for rapid unsupervised cryo-EM structure determination. Nat. Methods 14, 290–296. https://doi.org/10.1038/nmeth.4169.

72. Bell, J.M., Chen, M., Durmaz, T., Fluty, A.C., and Ludtke, S.J. (2018). New software tools in EMAN2 inspired by EMDatabank map challenge. J. Struct. Biol. 204, 283–290. https://doi.org/10.1016/j.jsb.2018.09.002.

73. Hohn, M., Tang, G., Goodyear, G., Baldwin, P.R., Huang, Z., Penczek, P.A., Yang, C., Glaeser, R.M., Adams, P.D., and Ludtke, S.J. (2007). SPARX, a new environment for Cryo-EM image processing. J. Struct. Biol. 157, 47–55. https://doi.org/10.1016/j.jsb.2006.07.003.

Cell
Article

OPEN ACCESS

74. Schneidman-Duhovny, D., Hammel, M., and Sali, A. (2010). FoXS: a web server for rapid computation and fitting of SAXS profiles. Nucleic Acids Res. *38*, W540–W544. https://doi.org/10.1093/NAR/GKQ461.

75. Suloway, C., Pulokas, J., Fellmann, D., Cheng, A., Guerra, F., Quispe, J., Stagg, S., Potter, C.S., and Carragher, B. (2005). Automated molecular microscopy: the new Leginon system. J. Struct. Biol. *151*, 41–60. https://doi.org/10.1016/j.jsb.2005.03.010.

76. Zheng, S.Q., Palovcak, E., Armache, J.-P., Verba, K.A., Cheng, Y., and Agard, D.A. (2017). MotionCor2: anisotropic correction of beam-induced motion for improved cryo-electron microscopy. Nat. Methods *14*, 331–332. https://doi.org/10.1038/nmeth.4193.

77. Lander, G.C., Stagg, S.M., Voss, N.R., Cheng, A., Fellmann, D., Pulokas, J., Yoshioka, C., Irving, C., Mulder, A., Lau, P.-W., et al. (2009). Appion: an integrated, database-driven pipeline to facilitate EM image processing. J. Struct. Biol. *166*, 95–102. https://doi.org/10.1016/j.jsb.2009.01.002.

78. Tan, Y.Z., Baldwin, P.R., Davis, J.H., Williamson, J.R., Potter, C.S., Carragher, B., and Lyumkis, D. (2017). Addressing preferred specimen orientation in single-particle cryo-EM through tilting. Nat. Methods *14*, 793–796. https://doi.org/10.1038/nmeth.4347.

79. Pettersen, E.F., Goddard, T.D., Huang, C.C., Couch, G.S., Greenblatt, D.M., Meng, E.C., and Ferrin, T.E. (2004). UCSF Chimera—a visualization system for exploratory research and analysis. J. Comput. Chem. *25*, 1605–1612. https://doi.org/10.1002/jcc.20084.

80. Adams, P.D., Afonine, P.V., Bunkóczi, G., Chen, V.B., Davis, I.W., Echols, N., Headd, J.J., Hung, L.-W., Kapral, G.J., Grosse-Kunstleve, R.W., et al. (2012). PHENIX: a comprehensive Python-based system for macromolecular structure solution. Acta Crystallogr. D Biol. Crystallogr. *66*, 213–221. https://doi.org/10.1107/S0907444909052925.

81. Emsley, P., Lohkamp, B., Scott, W.G., and Cowtan, K. (2010). Features and development of Coot. Acta Crystallogr. D Biol. Crystallogr. *66*, 486–501. https://doi.org/10.1107/S0907444910007493.

82. Holden, S.J., Uphoff, S., Hohlbein, J., Yadin, D., Le Reste, L., Britton, O.J., and Kapanidis, A.N. (2010). Defining the Limits of Single-Molecule FRET Resolution in TIRF Microscopy. Biophys. J. *99*, 3102–3111. https://doi.org/10.1016/J.BPJ.2010.09.005.

83. Ellis, B., Haaland, P., Hahne, F., Le Meur, N., Gopalakrishnan, N., Spidlen, J., Jiang, M., and Finak, G. (2024). flowCore: Basic structures for flow cytometry data. Bioconductor. http://bioconductor.org/packages/flowCore/.

84. Schindelin, J., Arganda-Carreras, I., Frise, E., Kaynig, V., Longair, M., Pietzsch, T., Preibisch, S., Rueden, C., Saalfeld, S., Schmid, B., et al. (2012). Fiji: an open-source platform for biological-image analysis. Nat. Methods *9*, 676–682. https://doi.org/10.1038/nmeth.2019.

85. Trapnell, C., Cacchiarelli, D., Grimsby, J., Pokharel, P., Li, S., Morse, M., Lennon, N.J., Livak, K.J., Mikkelsen, T.S., and Rinn, J.L. (2014). The dynamics and regulators of cell fate decisions are revealed by pseudotemporal ordering of single cells. Nat. Biotechnol. *32*, 381–386. https://doi.org/10.1038/nbt.2859.

86. Carpentier, G., Berndt, S., Ferratge, S., Rasband, W., Cuendet, M., Uzan, G., and Albanese, P. (2020). Angiogenesis Analyzer for ImageJ—A comparative morphometric analysis of "Endothelial Tube Formation Assay" and "Fibrin Bead Assay". Sci. Rep. *10*, 11568. https://doi.org/10.1038/s41598-020-67289-8.

87. Suarez-Arnedo, A., Torres Figueroa, F., Clavijo, C., Arbeláez, P., Cruz, J.C., and Muñoz-Camargo, C. (2020). An image J plugin for the high throughput image analysis of in vitro scratch wound healing assays. PLoS One *15*, e0232565. https://doi.org/10.1371/journal.pone.0232565.

88. Chaudhury, S., Lyskov, S., and Gray, J.J. (2010). PyRosetta: a script-based interface for implementing molecular modeling algorithms using Rosetta. Bioinformatics *26*, 689–691. https://doi.org/10.1093/bioinformatics/btq007.

89. Tegunov, D., and Cramer, P. (2019). Real-time cryo-electron microscopy data preprocessing with Warp. Nat. Methods *16*, 1146–1152. https://doi.org/10.1038/s41592-019-0580-y.

90. Rohou, A., and Grigorieff, N. (2015). CTFFIND4: Fast and accurate defocus estimation from electron micrographs. J. Struct. Biol. *192*, 216–221. https://doi.org/10.1016/j.jsb.2015.08.008.

91. Bepler, T., Morin, A., Rapp, M., Brasch, J., Shapiro, L., Noble, A.J., and Berger, B. (2019). Positive-unlabeled convolutional neural networks for particle picking in cryo-electron micrographs. Nat. Methods *16*, 1153–1160. https://doi.org/10.1038/s41592-019-0575-8.

92. Echols, N., Grosse-Kunstleve, R.W., Afonine, P.V., Bunkóczi, G., Chen, V.B., Headd, J.J., McCoy, A.J., Moriarty, N.W., Read, R.J., Richardson, D.C., et al. (2012). Graphical tools for macromolecular crystallography in PHENIX. J. Appl. Crystallogr. *45*, 581–586. https://doi.org/10.1107/S0021889812017293.

93. Schindelin, J., Rueden, C.T., Hiner, M.C., and Eliceiri, K.W. (2015). The ImageJ ecosystem: an open platform for biomedical image analysis. Mol. Reprod. Dev. *82*, 518–529. https://doi.org/10.1002/mrd.22489.

94. Carpenter, A.E., Jones, T.R., Lamprecht, M.R., Clarke, C., Kang, I.H., Friman, O., Guertin, D.A., Chang, J.H., Lindquist, R.A., Moffat, J., et al. (2006). CellProfiler: image analysis software for identifying and quantifying cell phenotypes. Genome Biol. *7*, R100. https://doi.org/10.1186/gb-2006-7-10-r100.

95. Stirling, D.R., Swain-Bowden, M.J., Lucas, A.M., Carpenter, A.E., Cimini, B.A., and Goodman, A. (2021). CellProfiler 4: improvements in speed, utility and usability. BMC Bioinformatics *22*, 433. https://doi.org/10.1186/s12859-021-04344-9.

96. Fontana, M., Fijen, C., Lemay, S.G., Mathwig, K., and Hohlbein, J. (2018). High-throughput, non-equilibrium studies of single biomolecules using glass-made nanofluidic devices. Lab Chip *19*, 79–86. https://doi.org/10.1039/C8LC01175C.

97. Srivatsan, S.R., McFaline-Figueroa, J.L., Ramani, V., Saunders, L., Cao, J., Packer, J., Pliner, H.A., Jackson, D.L., Daza, R.M., Christiansen, L., et al. (2020). Massively multiplex chemical transcriptomics at single-cell resolution. Science *367*, 45–51. https://doi.org/10.1126/SCIENCE.AAX6234.

98. Hao, Y., Hao, S., Andersen-Nissen, E., Mauck, W.M., 3rd, Zheng, S., Butler, A., Lee, M.J., Wilk, A.J., Darby, C., Zager, M., et al. (2021). Integrated analysis of multimodal single-cell data. Cell *184*, 3573–3587.e29. https://doi.org/10.1016/j.cell.2021.04.048.

99. Leutert, M., Rodríguez-Mias, R.A., Fukuda, N.K., and Villén, J. (2019). R2-P2 rapid-robotic phosphoproteomics enables multidimensional cell signaling studies. Mol. Syst. Biol. *15*, e9021. https://doi.org/10.15252/msb.20199021.

100. Navarrete-Perea, J., Yu, Q., Gygi, S.P., and Paulo, J.A. (2018). Streamlined Tandem Mass Tag (SL-TMT) Protocol: An Efficient Strategy for Quantitative (Phospho)proteome Profiling Using Tandem Mass Tag-Synchronous Precursor Selection-MS3. J. Proteome Res. *17*, 2226–2236. https://doi.org/10.1021/acs.jproteome.8b00217.

101. Schweppe, D.K., Eng, J.K., Yu, Q., Bailey, D., Rad, R., Navarrete-Perea, J., Huttlin, E.L., Erickson, B.K., Paulo, J.A., and Gygi, S.P. (2020). Full-Featured, Real-Time Database Searching Platform Enables Fast and Accurate Multiplexed Quantitative Proteomics. J. Proteome Res. *19*, 2026–2034. https://doi.org/10.1021/acs.jproteome.9b00860.

102. Eng, J.K., Jahan, T.A., and Hoopmann, M.R. (2013). Comet: an open-source MS/MS sequence database search tool. Proteomics *13*, 22–24. https://doi.org/10.1002/pmic.201200439.

103. Rad, R., Li, J., Mintseris, J., O'Connell, J., Gygi, S.P., and Schweppe, D.K. (2021). Improved Monoisotopic Mass Estimation for Deeper Proteome Coverage. J. Proteome Res. *20*, 591–598. https://doi.org/10.1021/acs.jproteome.0c00563.